

Regularized Estimation of Magnitude and Phase of Multi-Coil B_1 Field via Bloch-Siegert B_1 Mapping and Coil Combination Optimizations

Feng Zhao*, *Student Member, IEEE*, Jeffrey A. Fessler, *Fellow, IEEE*, Steven M. Wright, *Fellow, IEEE*, and Douglas C. Noll, *Senior Member, IEEE*

Abstract—Parallel excitation requires fast and accurate B_1 map estimation. Bloch-Siegert (BS) B_1 mapping is very fast and accurate over a large dynamic range. When applied to multi-coil systems, however, this phase-based method may produce low SNR estimates in low magnitude regions due to localized excitation patterns of parallel excitation systems. Also, the imaging time increases with the number of coils. In this work, we first propose to modify the standard BS B_1 mapping sequence so that it avoids the scans required by previous B_1 phase estimation methods. A regularized method is then proposed to jointly estimate the magnitude and phase of multi-coil B_1 maps from BS B_1 mapping data, improving estimation quality by using the prior knowledge of the smoothness of B_1 magnitude and phase. Lastly, we use Cramer-Rao Lower Bound analysis to optimize the coil combinations, to improve the quality of the raw data for B_1 estimation. The proposed methods are demonstrated by simulations and phantom experiments.

Index Terms—Magnetic Resonance Imaging (MRI), B_1 mapping, parallel excitation, Bloch-Sieget B_1 mapping, regularization, phase estimation, Cramer-Rao Lower Bound

I. INTRODUCTION

FOR MRI with parallel excitation (PEX), it is critical to rapidly and accurately estimate the magnitude and relative phase of the multi-channel B_1 field, also known as B_1^+ mapping. Numerous methods have been proposed to map B_1 magnitude, such as double-angle method [1], actual flip angle imaging (AFI) [2] and Bloch-Siegert (BS) B_1 mapping [3]. PEX pulse design also needs the relative phase maps, i.e., the phase of one coil relative to that of all the other coils, which is typically mapped by successively exciting the same object with each coil and receiving the signal by one common coil or one common set of coils.

The approach described in this paper uses the BS B_1 mapping method which applies an off-resonance RF pulse between the excitation pulse and the readout gradients [3].

This work was supported in part by the National Institutes of Health under Grant R01 NS58576 and Grant P01 CA87634. Asterisk indicates corresponding author.

*F. Zhao is with the Biomedical Engineering Department, The University of Michigan, Ann Arbor, MI 48109, USA (e-mail: zhaofll@umich.edu).

J. A. Fessler is with the Department of Electrical Engineering and Computer Science, The University of Michigan, Ann Arbor, MI 48109, USA (e-mail: fessler@umich.edu).

S. M. Wright is with the Department of Electrical and Computer Engineering, Texas A& M University, College Station, TX 77843, USA (e-mail: smwright@tamu.edu).

D. C. Noll is with the Biomedical Engineering Department, The University of Michigan, Ann Arbor, MI 48109, USA (e-mail: dnoll@umich.edu).

This off-resonance Bloch-Siegert (BS) pulse induces phase shifts that are proportional to $|B_1|^2$. The BS method is popular because it is fast and relatively accurate over a wide dynamic range and it is insensitive to T_1 , chemical shift, B_0 field inhomogeneity and magnetization transfer effects [3]. Its speed and wide dynamic range are especially beneficial for PEX systems where B_1 mapping is generally more time-consuming and has wider dynamic ranges than single channel systems. However, a disadvantage of this phase-based method is that the B_1 field estimation in low magnitude regions may suffer from low signal-to-noise ratio (SNR), due to insufficient excitation or low spin density. In particular, the problem of insufficient excitation is severe in PEX B_1 mapping because of the localized B_1 sensitivities of each coil. Furthermore, conventional estimation of B_1 phase needs another set of scans, which might be information redundant.

BS B_1 mapping for PEX has been improved in [4] by using combinations of multiple coils for imaging excitation. However, regions of low spin density and/or insufficient excitation may still be problematic, and estimation of B_1 phase still needs additional scans. Simply smoothing the noisy images with low-pass filters may propagate errors from the corrupted regions into neighboring regions. Therefore, we propose a modified BS B_1 mapping procedure that estimates both the magnitude and phase maps, avoiding the additional phase mapping scans required by conventional methods; then a regularized estimation method is proposed to jointly estimate the magnitude and relative phase of multi-coil B_1 maps from this BS B_1 mapping data. By utilizing the prior knowledge that B_1 maps are smooth, regularization can improve B_1 map estimation in low magnitude regions.

Many B_1 mapping methods, e.g., [4] [5] [6], use linear combinations of PEX channels to narrow the dynamic range of the effective B_1 field for better SNR, where typically all-but-one strategies are applied. However, these strategies are likely to be suboptimal in practice: the power levels of different channels in the object could be uneven due to non-isocenter positioning, which may cause nonuniform B_1 magnitude in the composite fields; the relative phase between channels could be far from what is assumed in those strategies, which may produce dark holes in the composite fields. Malik et al. proposed a method to optimize coil combinations for PEX B_1 mapping [7], but it optimized only over a single complex parameter of the combination matrix over a limited range empirically. That work evaluated the results according to two criteria: the

dynamic range of the composite B_1 maps and the condition number of the combination matrix, which sometimes are hard to balance and also may not indicate the estimation quality. In this paper, we propose to optimize linear coil combinations in [8] based on Cramer-Rao Lower Bound (CRLB) analysis [9]. The proposed method is general enough to optimize the combinations over all the elements of the coil combination matrix, providing the most flexibility for optimization. We evaluated the combinations directly based on the variance of the complex B_1 field estimates instead of indirect factors like dynamic ranges and condition numbers. The proposed approach minimizes the estimation variance of the pixel that has the maximal estimation variance, reducing the occurrence of focal noise amplification. Simulated Annealing (SA) [10] is used for this highly nonlinear optimization problem.

This paper is organized by starting with the signal model of images acquired by the proposed BS B_1 mapping sequence and then introducing the regularized estimation. We next demonstrate the proposed regularized method with simulation studies and phantom experiments at 3T. Section III considers optimization of the coil combinations using CRLB analysis, and then demonstrates the proposed methods by comparisons with the conventional all-but-one method and the method in [7] using simulation studies. Note that the regularized B_1 estimation algorithm in Section II and the coil combination optimization approach in Section III are relatively independent; these two methods may be combined, but neither of them requires the knowledge or results of the other.

II. REGULARIZED BS B_1 ESTIMATION

A. Linear Combinations of Coils in B_1 Mapping

Instead of mapping one coil at a time, we estimate the multi-channel B_1 field by acquiring standard BS B_1 mapping data with multiple coils turned on at each time [4]. Each composite complex B_1 field, $\tilde{C}_n(\mathbf{r})$, is a linear combination of the complex B_1 maps, $C_m(\mathbf{r})$, of the individual coils:

$$\tilde{C}_n(\mathbf{r}) = \sum_{m=1}^N \alpha_{n,m} C_m(\mathbf{r}) \quad (1)$$

where $n = 1, 2, \dots, N$, N is the number of channels available, \mathbf{r} denotes the spatial locations, and $\alpha_{n,m}$ is the user-defined complex scalar weighting for the m th individual coil in the n th scan. A convenient choice for $\alpha_{n,m}$ is the so-called all-but-one or leave-one-coil-out strategy, where $\alpha(n, n) = 0$ or -1 and $\alpha_{n,m} = 1$ when $m \neq n$ [5] [11]. Both the composite complex B_1 maps and the individual complex B_1 maps can be expressed in terms of their magnitudes and phases:

$$\tilde{C}_n(\mathbf{r}) = \tilde{B}_n(\mathbf{r}) e^{i\tilde{\phi}_n(\mathbf{r})}, C_m(\mathbf{r}) = B_m(\mathbf{r}) e^{i\phi_m(\mathbf{r})}. \quad (2)$$

B. The Signal Model

Standard BS B_1 mapping applies the BS pulse after the regular excitation pulse [3]. This method typically needs 2 scans for each coil to measure B_1 magnitude, thus $2N$ scans are needed for an N -channel PEX system. To estimate both B_1 magnitude and relative phase by the standard BS B_1 mapping without additional scans for phase, we propose to use the

same coil combinations for the BS pulse and the corresponding excitation pulse. The signal models for the noiseless BS data (reconstructed images) of the N pairs of scans, i.e., $\tilde{S}_n^+(\mathbf{r})$ and $\tilde{S}_n^-(\mathbf{r})$, are described as follows:

$$\begin{cases} \tilde{S}_n^+(\mathbf{r}) = \sin(\mu \tilde{B}_n(\mathbf{r})) e^{i\tilde{\phi}_n(\mathbf{r})} m_n^+(\mathbf{r}) e^{i\phi_b(\mathbf{r})} e^{iK_{BS}^+(\mathbf{r}) \tilde{B}_n^2(\mathbf{r})} \\ \tilde{S}_n^-(\mathbf{r}) = \sin(\mu \tilde{B}_n(\mathbf{r})) e^{i\tilde{\phi}_n(\mathbf{r})} m_n^-(\mathbf{r}) e^{i\phi_b(\mathbf{r})} e^{iK_{BS}^-(\mathbf{r}) \tilde{B}_n^2(\mathbf{r})} \end{cases} \quad (3)$$

where $n = 1, 2, \dots, N$, and as described in (2), $\tilde{B}_n(\mathbf{r})$ and $\tilde{\phi}_n(\mathbf{r})$ denote the magnitude and phase of the composite B_1 fields respectively; the superscripts \pm denote the scan that has the BS pulse with $\pm\omega_{RF}$ off-resonance frequency, μ is the ratio between the actual flip angle and $\tilde{B}_n(\mathbf{r})$, $m_n^\pm(\mathbf{r})$ is the magnetization related to spin density, T_1 , T_2 , T_R , T_E , flip angle, receive sensitivity, magnetization transfer (MT) effect, etc., $\phi_b(\mathbf{r})$ is the corresponding unknown background phase, and $K_{BS}^\pm(\mathbf{r})$ is the BS pulse constant that incorporates the B_0 field map [3]:

$$K_{BS}^\pm(\mathbf{r}) = \frac{1}{2} \int_0^T \frac{(\gamma B_{\text{normalized}}(t))^2}{\pm\omega_{RF}(t) - \omega_0(\mathbf{r})} dt \quad (4)$$

where $B_{\text{normalized}}(t)$ is the normalized shape of the BS pulse. Due to the asymmetric MT effect [12], $m_n^+(\mathbf{r})$ is slightly different from $m_n^-(\mathbf{r})$. Moreover, we model additive independent and identically distributed (i.i.d.) complex Gaussian noise, i.e., $\epsilon_n^\pm(\mathbf{r})$, to the signal, and simplify (3) by changing variables:

$$\begin{cases} S_n^+(\mathbf{r}) = M_n^+(\mathbf{r}) e^{i[K_{BS}^+(\mathbf{r}) \tilde{B}_n^2(\mathbf{r}) + \tilde{\phi}'_n(\mathbf{r})]} + \epsilon_n^+(\mathbf{r}) \\ S_n^-(\mathbf{r}) = M_n^-(\mathbf{r}) e^{i[K_{BS}^-(\mathbf{r}) \tilde{B}_n^2(\mathbf{r}) + \tilde{\phi}'_n(\mathbf{r})]} + \epsilon_n^-(\mathbf{r}) \end{cases} \quad (5)$$

where $S_n^\pm(\mathbf{r})$ are the noisy images from the n th pair of scans, $M_n^\pm(\mathbf{r}) \triangleq \sin(\mu \tilde{B}_n(\mathbf{r})) m_n^\pm(\mathbf{r})$, and $\tilde{\phi}'_n(\mathbf{r}) \triangleq \tilde{\phi}_n(\mathbf{r}) + \phi_b(\mathbf{r})$. The simplest way to estimate B_1 magnitude and phase from this set of data is to first obtain $\tilde{B}_n(\mathbf{r})$ using the standard BS B_1 mapping estimator [3], and then, given $B_n(\mathbf{r})$, the relative B_1 phase, $\tilde{\phi}'_n(\mathbf{r})$, can be derived by maximum likelihood estimator of (5) or simply taking:

$$\tilde{\phi}'_n(\mathbf{r}) = \angle [S_n^+(\mathbf{r}) / e^{iK_{BS}^+(\mathbf{r}) \tilde{B}_n^2(\mathbf{r})}] \quad (6)$$

where $M_n^\pm(\mathbf{r})$ is not needed. We propose to set the coil combination of each excitation pulse the same as its corresponding BS pulse, so that $\tilde{B}_n(\mathbf{r})$ and $\tilde{\phi}'_n(\mathbf{r})$ correspond to the same composite B_1 map, hence the individual B_1 magnitude and phase, i.e., $B_n(\mathbf{r})$ and $\phi'_n(\mathbf{r})$, can be derived by (9) below. This is how the modified BS sequence can avoid the additional scans for B_1 phase. For regularized estimation, $M_n^\pm(\mathbf{r})$ is a set of nuisance parameters that we must jointly estimate, but they are fortunately linear terms that can be easily estimated.

C. Regularized Estimation of B_1 Magnitude and Phase

Regularization enforces prior knowledge to improve estimation. It is reasonable to assume that the complex B_1 fields of the individual coils, i.e., $B_m(\mathbf{r}) e^{i\phi_m(\mathbf{r})}$, are spatially smooth. As shown in the signal models (5), the B_1 magnitude and phase are separate, and the fields of the individual coils are superimposed with each other due to the coil combinations. Thus, it is easier to estimate magnitude and phase of the composite B_1 fields separately [13], even though the regularization

is for the complex fields of the individual coils. Grouping all discretized spatially varying maps into column vectors (shown in bold fonts), we proposed regularized maximum-likelihood estimation by minimizing the following cost function:

$$\begin{aligned} \Psi(\tilde{\mathbf{B}}, \tilde{\phi}, \mathbf{M}) = & \sum_{n=1}^N \sum_{\varsigma=+,-} \|\mathbf{S}_n^\varsigma - \mathbf{M}_n^\varsigma \odot e^{i(\mathbf{K}_{BS}^\varsigma \odot \tilde{\mathbf{B}}_n^2 + \tilde{\phi}'_n)}\|^2 \\ & + \beta \sum_{n=1}^N \|C(\mathbf{B}_n \odot e^{i\phi'_n})\|^2 \end{aligned} \quad (7)$$

where β is the scalar regularization parameter, \mathbf{M} is the concatenation of the image magnitude vectors \mathbf{M}_n^\pm of all channels, $\tilde{\mathbf{B}}$ and $\tilde{\phi}$ denote the concatenation of all the composite B_1 magnitudes $\tilde{\mathbf{B}}_n$ and all the composite B_1 phases $\tilde{\phi}'_n$, respectively, " \odot " denotes element-by-element multiplication between vectors, $\tilde{\mathbf{B}}_n^2$ denotes the vector that contains the squares of the corresponding elements of $\tilde{\mathbf{B}}_n$, \mathbf{B}_n and ϕ'_n denote the individual B_1 magnitudes and phases respectively, and C is a multi-dimensional finite differencing matrix used to penalize roughness. For simplicity of the expression in (7), we do not show the inherent relation between $\tilde{\mathbf{B}}_n e^{i\tilde{\phi}'_n}$ and $\mathbf{B}_n e^{i\phi'_n}$ in the regularization term, which is shown in (9). Note that the units of the data fit term may be arbitrarily different for different scans, and the regularization term can also have different units. To make it easier to choose a value of β that works for different scans, we normalize the data \mathbf{S}_n^ς in (7) so that \mathbf{S}_1^+ has unit norm, and we always use units μT for \mathbf{B}_n . This ensures that β always has consistent units ($1/\mu\text{T}^2$).

We iteratively minimize the cost function (7) by cyclically updating $\tilde{\mathbf{B}}$, $\tilde{\phi}$ and \mathbf{M} :

$$(\hat{\tilde{\mathbf{B}}}, \hat{\tilde{\phi}}, \hat{\mathbf{M}}) = \underset{\tilde{\mathbf{B}}, \tilde{\phi} \in \mathbb{R}^{(NN_p) \times 1}, \mathbf{M} \in \mathbb{R}^{(2NN_p) \times 1}}{\text{argmin}} \Psi(\tilde{\mathbf{B}}, \tilde{\phi}, \mathbf{M}) \quad (8)$$

where $\hat{\tilde{\mathbf{B}}}$, $\hat{\tilde{\phi}}$ and $\hat{\mathbf{M}}$ denote the estimates of $\tilde{\mathbf{B}}$, $\tilde{\phi}$, \mathbf{M} respectively, and N_p is the number of pixels of each channel. We update \mathbf{M} , which is a real unknown, by simply taking the real least-squares solution of (7) in each iteration. The cost function is non-quadratic in $\tilde{\mathbf{B}}$ and $\tilde{\phi}$, so we use conjugate gradients with backtracking line search algorithms (BCG-LS) [13] [14] to update $\tilde{\mathbf{B}}$ and $\tilde{\phi}$ respectively. The standard approach [3] produces a good initial guess for $\tilde{\mathbf{B}}$, and then we compute the initial guess of $\tilde{\phi}$ using (6). The stopping criterion for this optimization algorithm is to check whether the change of the cost function Ψ between two consecutive iterations is smaller than a certain value. Once $\tilde{\mathbf{B}}$ and $\tilde{\phi}$ are estimated, magnitude and relative phase maps of the original coils, \mathbf{B} and ϕ , are derived easily using the following relation:

$$\begin{bmatrix} B_1(\mathbf{r})e^{i\phi'_1(\mathbf{r})} \\ \vdots \\ B_N(\mathbf{r})e^{i\phi'_N(\mathbf{r})} \end{bmatrix} = A^{-1} \begin{bmatrix} \tilde{B}_1(\mathbf{r})e^{i\tilde{\phi}'_1(\mathbf{r})} \\ \vdots \\ \tilde{B}_N(\mathbf{r})e^{i\tilde{\phi}'_N(\mathbf{r})} \end{bmatrix} \quad (9)$$

where $\phi'_n(\mathbf{r}) \triangleq \phi_n(\mathbf{r}) + \phi_b(\mathbf{r})$, which does not change the

relative phase maps, and A is the coil combination matrix:

$$A \triangleq \begin{bmatrix} \alpha_{1,1} & \dots & \alpha_{1,N} \\ \vdots & \ddots & \vdots \\ \alpha_{N,1} & \dots & \alpha_{N,N} \end{bmatrix}. \quad (10)$$

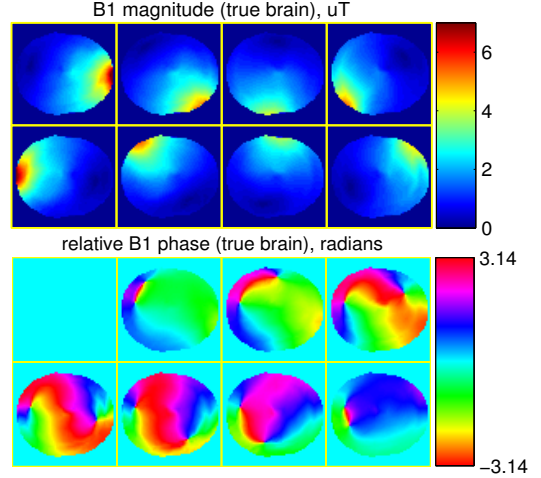


Fig. 1. B_1 maps of a head, used as the ground truth in simulation study.

D. Simulation Study

We performed a simulation study to demonstrate the proposed BS B_1 mapping sequence and the corresponding regularized B_1 estimation method. First, a finite-difference time-domain (FDTD) simulation generated 2D magnetic fields of an eight-channel parallel excitation array for brain imaging at 3T, which were used as the true B_1 maps in the simulations (shown in Fig. 1). We used a set of brain tissue parameter maps, e.g., T_1 map, T_2 map and spin densities, from BrainWeb database [15]–[19] as the true values for generating images produced by the BS sequence. The image magnitude was generated based on the signal equation of spoiled gradient echo (SPGR) sequence that is shown below in (17) with flip angle = 20° , $T_R = 200$ ms, $T_E = 10$ ms. We then used Bloch equation simulations to generate the image phase based on ± 4 kHz off-resonance Fermi BS pulses ($K_{BS} = 76.9 \text{ rad/G}^2$) and a realistic B_0 field map acquired from a head scan on a 3T GE scanner (ranging from -86 Hz to 25 Hz). We combined the B_1 fields with the all-but-one strategy with $\alpha_{1,1} = -1, \alpha_{1,2} = \dots = \alpha_{1,N} = 1$. Adding i.i.d. complex Gaussian noise to the noiseless images, we simulated the raw data in image domain acquired by SPGR-based BS B_1 mapping sequence with the proposed modifications, and the SNR of the raw data was around 34 dB. The SNR is defined in image domain as:

$$\text{SNR} = 20 \log_{10} \left(\frac{\|\mathbf{S}_t\|}{\|\mathbf{S}_t - \mathbf{S}\|} \right) \quad (11)$$

where \mathbf{S}_t and \mathbf{S} denote the noise-free and noisy images respectively. Each method was applied to datasets for 20 instances of random noise. The matrix size of each 2D image is 64×64 , and field of view is $24 \text{ cm} \times 24 \text{ cm}$. Moreover,

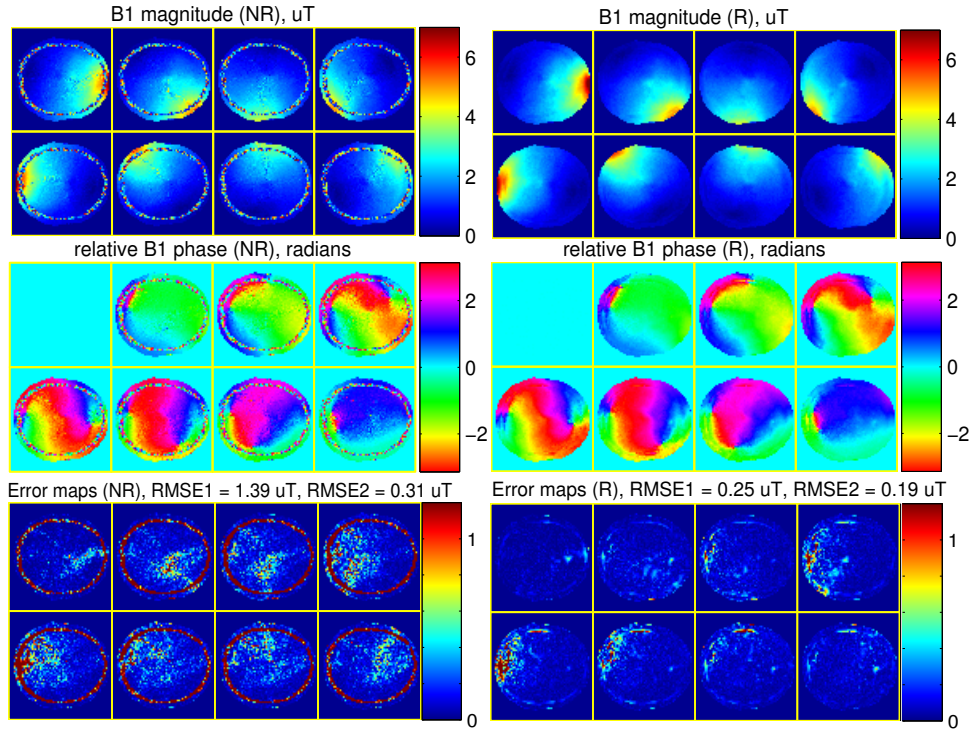


Fig. 2. The estimated B_1 magnitude (top row), phase (middle row) maps and the error (bottom row) maps by the non-regularized (NR) method (left) and the regularized (R) method (right) using conventional all-but-one coil combination scans, in simulation study.

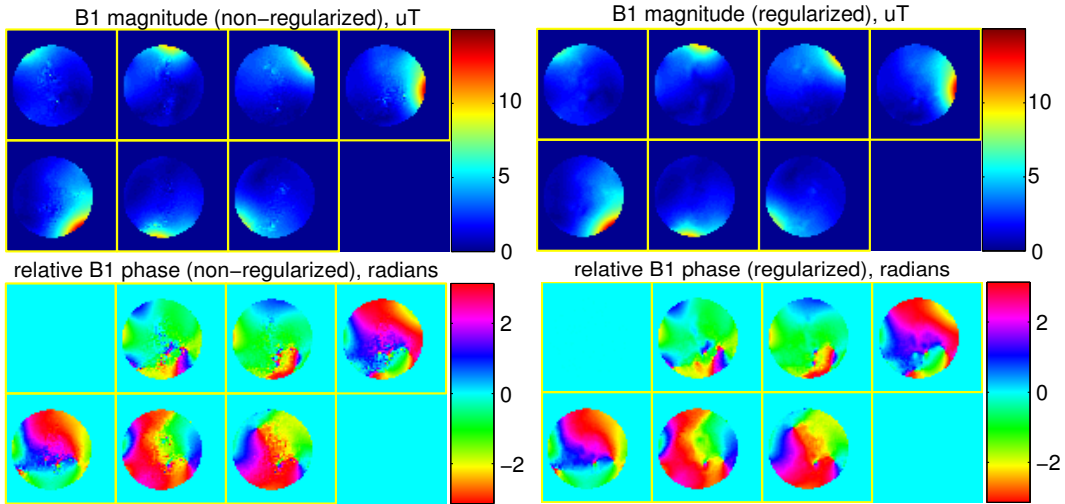


Fig. 3. The estimated B_1 magnitude (top) and phase (bottom) maps by the non-regularized method (left) and the regularized method (right), in phantom study.

estimator (8) uses a mask in the image domain to eliminate space outside the object. This mask can be obtained from the images acquired for the B_0 mapping or the BS images.

Using these simulated raw coil images, we compared the proposed regularized B_1 estimation method with standard non-regularized methods for B_1 magnitude and phase. For the proposed method, we manually selected the regularization parameter to be $\beta = 0.15$. The matrix C in (7) was a second-order 2D finite differencing matrix. Fig. 2 shows the reconstructed B_1 magnitude and phase maps produced by the

standard non-regularized method and the proposed regularized method for one instance of random noise. Fig. 2 also shows the error maps of the complex B_1 maps, i.e., $|\hat{\mathbf{B}} \odot e^{i\hat{\phi}} - \mathbf{B} \odot e^{i\phi}|$ for each method, where each pixel value is the average error magnitude over the 20 instances of random noise. All the images in Fig. 2 are displayed with the mask used in the optimization. Based on these images, we also computed the root mean square error (RMSE) for each complex B_1 map:

$$\text{RMSE} \triangleq \frac{\|\hat{\mathbf{B}} \odot e^{i\hat{\phi}} - \mathbf{B} \odot e^{i\phi}\|}{\sqrt{N_p}}. \quad (12)$$

We calculated the RMSE values both with the mask used in the optimization and a more accurate mask obtained from the true brain image respectively, and they are denoted as RMSE_1 and RMSE_2 respectively. The latter mask excludes signal-free regions within the former mask, which is the skull region, because the skull region may dominate RMSE_1 in some methods but it is less important for pulse design. Fig. 2 shows those RMSEs (averaged over the 20 instances of random noise) in the figure titles of the error maps. Compared to the non-regularized method, the proposed regularized B_1 estimation produced less noisy B_1 maps that have significantly smaller errors.

E. Phantom Experiments

We performed phantom experiments to demonstrate the proposed regularized BS B_1 map estimation on a 3T GE scanner (GE Healthcare, Milwaukee, WI, USA) equipped with an 8-channel custom parallel transmit/receive system [20] [21]. We used a spherical phantom filled with distilled water. Due to a failure in one RF amplifier, only seven of the transmit channels were used; the eighth has zero input throughout the experiment. All the data were acquired with a SPGR sequence having a 2D spin-warp readout. We applied a 20 ms Fermi BS pulse with ± 4 kHz off-resonance frequencies. Other imaging parameters were: $T_E = 23$ ms, $T_R = 200$ ms, $\text{FOV} = 24 \times 24$ cm, 64×64 reconstruction matrix size, and axial slice imaging. The eight-channel parallel imaging data produces one image per channel using FFT reconstruction. Each set of eight-channel images were then combined into single-channel images by a weighted summation across channels. Each channel has one scalar complex weight. Based on a set of receive sensitivity maps acquired off-line, the weights were adjusted to produce a homogeneous receive sensitivity, which is analogous to RF shimming for a homogeneous transmit sensitivity [22].

We first acquired a B_0 map (ranges from -80 to 8 Hz) using two 2D SPGR scans with an echo time difference 2.5 ms. A total of 14 proposed BS B_1 mapping scans were acquired for 7-channel B_1 estimation, where we applied the all-but-one coil combination with $\alpha_{1,1} = 0, \alpha_{1,2} = \dots = \alpha_{1,N} = 1$. The reconstructed raw images were then put into the standard non-regularized BS estimator and the proposed regularized BS estimator (8). For the proposed method, we manually selected the regularization parameter to be $\beta = 4$, and the matrix C in (7) was second-order 2D finite differencing matrix. A mask obtained from the SPGR image used for B_0 mapping was applied to the estimation. The whole reconstruction took less than a minute on a computer with Intel Core i5 CPU @ 2.5 GHz, 4 GB RAM and Matlab 8.1. Fig. 3 shows the estimated B_1 magnitude and phase maps, where the mask used for the estimation is applied to all the images. The proposed regularized estimation improves the quality of both the magnitude and phase maps. However, there are still several rough spots in the magnitude maps that were corrupted by the low signal intensity regions so much that they were not fully smoothed by the regularized algorithm. This is the main motivation for us to propose coil combination optimization, to

obtain better raw data for B_1 estimation, as discussed in the next section.

III. COIL COMBINATION OPTIMIZATION

A. Approximate Signal Model

The coil combination matrix A in (10) is conventionally chosen by an all-but-one strategy, but this approach is unlikely to be optimal in practice. Therefore, we propose a method to optimize the matrix A to improve the quality of the raw data for estimating the magnitude and phase of B_1 field in PEX. We use the CRLB to derive a lower bound on the variance of the complex B_1 field estimates in terms of the coil combination matrix A and then find the A that minimizes the worst-case noise-to-signal ratio (NSR).

To simplify the CRLB analysis, we make some approximations for (5): asymmetric MT effect is ignored so that $M_n^+(\mathbf{r}) \approx M_n^-(\mathbf{r}) \triangleq M_n(\mathbf{r})$, and the off-resonance effects in $K_{BS}^\pm(\mathbf{r})$ are ignored so that $K_{BS}^+(\mathbf{r}) \approx -K_{BS}^-(\mathbf{r}) \triangleq K$, which is a scalar constant. Assuming the real and imaginary parts of the i.i.d. Gaussian noise are uncorrelated and distributed as $\mathcal{N}(0, \sigma^2)$ where σ^2 is the variance, then the approximate distributions of the signals for each pixel are expressed as follows:

$$\begin{cases} S_r^+ \sim \mathcal{N}(M \cos(KB^2 + \phi), \sigma^2) \\ S_i^+ \sim \mathcal{N}(M \sin(KB^2 + \phi), \sigma^2) \\ S_r^- \sim \mathcal{N}(M \cos(-KB^2 + \phi), \sigma^2) \\ S_i^- \sim \mathcal{N}(M \sin(-KB^2 + \phi), \sigma^2) \end{cases} \quad (13)$$

where the subscripts n , indices \mathbf{r} , primes and tildes in (5) are omitted for simplicity, subscripts r/i denote the real/imaginary parts.

B. Cramel-Rao Lower Bound Analysis

The CRLB is a lower bound on the covariance of any unbiased estimator under certain regularity conditions. Although the nonlinear regularized estimator (8) is biased in general, even when $\beta = 0$, it is still desirable to minimize the CRLB to pursue improved data quality.

Equation (13) can be vectorized as follows:

$$\mathbf{y} = \boldsymbol{\mu}(\boldsymbol{\theta}) + \boldsymbol{\epsilon} \quad \text{where } \boldsymbol{\epsilon} \sim \mathcal{N}(\mathbf{0}, \sigma^2 \mathbf{I}) \quad (14)$$

where $\mathbf{y} = [S_r^+, S_i^+, S_r^-, S_i^-]^T$, $\boldsymbol{\mu} = [M \cos(KB^2 + \phi), M \sin(KB^2 + \phi), M \cos(-KB^2 + \phi), M \sin(-KB^2 + \phi)]^T$, $\boldsymbol{\theta} = [B, \phi]^T$. The Appendix verifies that this problem satisfies the regularity condition for the CRLB theorem. Using a Taylor expansion and assuming the scans have independent noise, the Appendix derives the lower bound of the variances of the complex B_1 estimates of the N channels in location \mathbf{r} :

$$\begin{aligned} \text{var}(\hat{C}_{n,\mathbf{r}}(A)) &\triangleq \text{var}(\hat{B}_{n,\mathbf{r}}(A)e^{i\hat{\phi}'_{n,\mathbf{r}}(A)}) \geq V_{n,\mathbf{r}}(A) \\ &\triangleq \{A^{-1} \text{diag}\left\{\frac{\sigma^2}{2M_{n,\mathbf{r}}^2(A)}[\tilde{B}_{n,\mathbf{r}}^2(A) + \frac{1}{4K^2 \tilde{B}_{n,\mathbf{r}}^2(A)}]\right\}A^{-H}\}_{n,n} \end{aligned} \quad (15)$$

where $n = 1, \dots, N$, $\text{diag}\{z\}$ denotes the diagonal matrix with vector z its diagonal entries, and we have put back the

subscripts n , indices \mathbf{r} , primes and tildes in (5) except that we move the indices \mathbf{r} to the subscripts and make A be the argument, as A is the main unknown of the coil combination optimization problem.

C. Optimize Linear Combinations of Array Elements

We optimize the SNR of the B_1 estimates by minimizing the lower bound of NSR, defined as the ratio between $\sqrt{V_{n,\mathbf{r}}(A)}$ and $B_n(\mathbf{r})$. Since (15) is only for one single pixel, a scalar that evaluates the noise performance of the whole 2D or 3D B_1 field of the N coils must be chosen for optimizing over the coil combination matrix A . To suppress the focal noise amplifications that are common in PEX B_1 mapping, we apply a min-max optimization strategy by minimizing the maximal $V_{n,\mathbf{r}}(A)$ over all spatial locations and channels to optimize the worst noise performance of the whole estimation. A practical issue is that PEX systems have amplitude limits that bound the maximum magnitude of the elements of A . Therefore, the final expression of this optimization problem is:

$$\hat{A} = \underset{A \in \mathbb{C}^{N \times N}}{\operatorname{argmin}} \max_{n,\mathbf{r}} \frac{\sqrt{V_{n,\mathbf{r}}(A)}}{B_n(\mathbf{r})} \quad (16)$$

subject to

$$\max_{m,n} |\alpha_{m,n}| \leq \lambda$$

where λ is the amplitude limit of the PEX system. This method optimizes the noise performance over all the elements $\alpha_{m,n}$ of A , which is much more flexible than the method in [7].

The cost function in (16) is highly nonlinear and nonconvex in terms of A , so it would be very hard to find the global minimum. In practice, however, it should suffice to keep the noise level below a certain reasonable value rather than to exhaustively search for the global minimizer. Since A is relatively a small matrix, we found that the Simulated Annealing (SA) method [10] in Matlab's Optimization Toolbox can efficiently find a reasonably good local minimum.

The CRLB expression (15) depends not only on the coil combination matrix A , but also on other parameter maps that are not known, namely $M_{n,\mathbf{r}}(A)$ and $\tilde{B}_{n,\mathbf{r}}(A)$. The composite maps $\tilde{B}_{n,\mathbf{r}}(A)$ can be described as:

$$\tilde{B}_{n,\mathbf{r}}(A) = \left| \sum_{m=1}^N \alpha_{n,m} B_m(\mathbf{r}) e^{i\phi_m(\mathbf{r})} \right|. \quad (17)$$

The maps $M_{n,\mathbf{r}}(A)$ depend on other parameters that are unknown, such as T_1 , T_2 and spin density, and can be modeled mathematically according to the specific imaging sequence. In this paper, we focus on the SPGR based BS sequence, where $M_{n,\mathbf{r}}(A)$ can be expressed as follows [23]:

$$M_{n,\mathbf{r}}(A) = B_1^-(\mathbf{r}) e^{-\frac{T_E}{T_2(\mathbf{r})}} \frac{\rho(\mathbf{r}) (1 - e^{-\frac{T_R}{T_1(\mathbf{r})}}) \sin(\mu \tilde{B}_{n,\mathbf{r}}(A))}{1 - e^{-\frac{T_R}{T_1(\mathbf{r})}} \cos(\mu \tilde{B}_{n,\mathbf{r}}(A))} \quad (18)$$

where $B_1^-(\mathbf{r})$ is the receive coil sensitivity map, $\rho(\mathbf{r})$ is the spin density map, $T_1(\mathbf{r})$ and $T_2(\mathbf{r})$ are the T_1 and T_2 maps respectively. Instead of attempting to determine these maps, which would be impractical, we use uniform maps with nominal T_1 , T_2 , and ρ values for optimizing A . For $B_1^-(\mathbf{r})$,

we either use uniform values when signal is received by a single coil in a non-high field scanner ($\leq 3T$), or acquire an off-line phantom data for a coarse estimation of $B_1^-(\mathbf{r})$. For the transmit B_1 magnitude, $B_m(\mathbf{r})$, we use a set of B_1 maps estimated by a phantom off-line. For the transmit B_1 phase, $\phi_m(\mathbf{r})$, we either use off-line phantom estimates or fast on-line low resolution *in-vivo* B_1 phase maps.

For our experiments, we focus on an eight-channel PEX head array that has 8-fold rotational symmetry, so although the proposed method can optimize over all the elements of A , it is natural to restrict the 8×8 matrix A to be circulant, saving computation time by reducing the number of unknowns to 8. This approach also seems to be more robust to local minima compared to optimizing all elements of A .

D. Simulation Study

In this study, we used the same reference B_1 maps generated by FDTD simulation in the section II-D (shown in Fig. 1). We also used the same set of brain tissue parameter maps used in Section II-D as the true values for generating images produced by the BS sequence. The image magnitude was generated based on the signal equation of SPGR sequence (17) with $T_R = 200$ ms, $T_E = 10$ ms. The BS induced phase was simulated based on 8 ms ± 4 kHz off-resonance Fermi BS pulses ($K_{BS} = 76.9$ rad/G²) and a realistic B_0 field map acquired from a brain on a 3T GE scanner (ranging from -86 Hz to 25 Hz). Furthermore, the B_1^- map was acquired from a real single-channel body receive coil of the 3T GE scanner. By adding i.i.d. complex Gaussian noise to the noiseless images generated based on (3), (17) and (18), we simulated the raw data in image domain acquired by SPGR-based BS B_1 mapping sequence. The matrix size of these 2D images is 64×64 . Note that the coil combination matrix A has to be optimized before simulating the raw data. In the data simulation, the standard deviation of the Gaussian noise stayed the same and the SNR of raw image data ranged from 23 dB to 26 dB depending on the specific coil combinations.

We used approximated parameters for the coil optimization step (16). T_2 and spin density were uniform maps with nominal values, as the absolute values of them do not affect the optimization of (16); T_1 maps were set to be the maximal value (2.6 s) of brain tissue. Since the true receive coil sensitivity map, which was acquired from a single-channel at 3T, is relatively uniform, we used a uniform B_1^- map for the optimization. Furthermore, we performed another FDTD simulation for a uniform phantom using the same coil configurations as we used for the brain simulation. The relative permittivity and conductivity of the phantom were set to be the corresponding average values of brain tissue, that is, 42.3 and 0.489 S/m respectively. The phantom had uniform spin density over the same spatial regions occupied by the brain in the previous FDTD simulation, and we cropped the phantom B_1 maps to match the brain shape for the optimization (shown in Fig. 4). For the B_1 phase specifically, in addition to using the phantom B_1 phase, which will be called "method 1", we also simulated a set of on-line low resolution (32×32 matrix) fast scans of the brain using one transmit coil at a time to obtain the

relative B_1 phase, which will be called "method 2". Moreover, for comparison purposes, we also simulated the case where we optimized the coil combinations based on the true B_1 maps as well as true B_1 -, T_1 , T_2 and spin density maps, called "oracle method". Table I summarizes the proposed methods. Circulant structure was assumed for the matrix A , and the optimization algorithm was initialized with the all-but-one combination. The threshold λ in (16) was set such that the RF power does not exceed a fixed peak nominal power. Furthermore, a fast low resolution prescan of the subject was simulated for defining a mask for the optimization. For illustration and analysis, a more accurate mask extracted from the true brain image was applied to all the images shown and computed the statistics for this simulation.

For comparison, we also simulated the results of the all-but-one combination with $\alpha_{1,1} = -1, \alpha_{1,2} = \dots = \alpha_{1,N} = 1$ and the method proposed by Malik et al. [7]. For Malik's method, we investigated the diagonal entry $\alpha e^{i\beta}$ within the range suggested in [7], i.e., $-11 < \alpha < 11$ and $-\pi/2 < \beta < \pi/2$, while keeping the off-diagonal entries to be 1. The B_1 mapping simulations for this method were also based on the SPGR-based BS B_1 mapping mentioned above. The optimal choice of $\alpha e^{i\beta}$ was chosen by minimizing RMSE between the reconstructed complex B_1 maps and the corresponding truth.

Fig. 5 shows the coil combination coefficients selected by the different methods. As we assumed circulant structure, only the first rows of each A , which are vectors of 8 complex numbers, are shown in the complex plane. Compared to the all-but-one method and Malik's method, all the other optimized results are scattered more uniformly within the complex plane and also "random-like". Fig. 6 shows the condition numbers of all the combination matrices and the corresponding composite B_1 magnitude maps. The results of "oracle method" and "method 2" have the smallest condition number, and both Malik's method and "method 1" reduced the condition number of the combination matrix compared to the all-but-one method. The composite B_1 magnitude maps show that "oracle method" and "method 2" significantly improved the low intensity regions, especially around the center where the intensity is low in all the composite maps of the all-but-one method. Based on the results of combination numbers and the composite B_1 maps, one may expect "oracle method" and "method 2" perform better than the other three methods.

We then simulated the B_1 map estimation with the five different coil combinations, where we used the non-regularized method to estimate the B_1 magnitude and phase. Fig. 7 shows the resulting B_1 magnitude and phase maps for one instance of random noise, and Fig. 8 also shows the error maps of the complex B_1 maps, i.e., $|\hat{B} \odot e^{i\phi} - B \odot e^{i\phi}|$, where each pixel value is the average error magnitude over the 20 instances of random noise. As predicted, "method 2" and "oracle method" produced less noisy B_1 maps than the other three methods. Despite the model mismatch mainly in B_1 magnitude, receive sensitivities and distributions of spin density, T_1 and T_2 , "method 2" still worked similarly well as "oracle method". In contrast, although "method 1" still improved the B_1 estimation compared to the all-but-one method, it did not perform as well as "method 2" and "oracle method". Moreover, due to

the limited flexibility in Malik's method, it did not improve B_1 estimation as much as "method 2" and "oracle method". The bottom-right part of Fig. 8 shows the RMSEs over all the pixels, defined in (12), of the complex B_1 maps reconstructed by the five methods; specifically, it shows the averaged RMSEs of the 20 instances of random noise and the corresponding error bars (shown on top of the averaged RMSE bars).

This empirical comparison illustrates that the proposed coil combination optimization can improve the SNR of multi-coil B_1 magnitude and phase estimation. Moreover, the proposed methods generally outperform Malik's method which optimizes only the diagonal entry of A . In addition, the proposed methods are robust to inaccurate magnitude related parameters, e.g., B_1 magnitude, receive sensitivities and distributions of spin density, T_1 and T_2 . However, unlike the B_1 magnitude estimated by phantom, B_1 phase estimates from phantom were far from the true B_1 phase in brain, causing the inferior performance of "method 1". With such big B_1 phase mismatch, the improvement of "method 1" over the all-but-one method is mainly from the optimization of the matrix condition number. Since a set of low resolution B_1 phase maps takes very minimal scan time in practice, we conclude that "method 2" is the more robust and practical method for the coil combination optimization.

IV. DISCUSSION AND CONCLUSION

We have proposed methods to improve BS B_1 mapping for parallel excitation pulse design in the following two main aspects: **Estimation quality**: the regularized method is proposed to jointly estimate the magnitude and phase of multi-coil B_1 maps from BS B_1 mapping data, improving estimation quality by using the smoothness of B_1 magnitude and phase; **Raw data quality**: the coil combination optimization based on CRLB analysis is proposed to optimize the SNR of the non-regularized complex B_1 estimation over the whole combination matrix. Furthermore, a minor improvement from the proposed method is that it avoids the B_1 phase mapping scans that are required for conventional methods.

The cost function for regularized B_1 estimation is non-convex, but our experiments have shown that initializing by applying the standard BS B_1 mapping and solving (3) is adequate to obtain a good local minimum with our gradient-based optimization algorithm. The CG-BLS algorithm efficiently optimizes the highly nonlinear cost function; a future work can be to design monotonic line search updates to further improve the algorithm efficiency [24]. One disadvantage of regularized estimation is that the regularization parameter is generally difficult to select automatically. In our implementation, the regularization parameters were chosen empirically. Theoretically, the regularization parameters control the spatial resolution of the reconstructed images, so one can select the regularization parameters automatically based on spatial resolution analysis [25]. Furthermore, based on our experience, the proposed algorithm generally converges quickly with 40-120 iterations and 2-3 subiterations depending on the noise level of the initial images.

The modified BS sequence produces a minor improvement on scan time by avoiding the B_1 phase mapping scans, but

TABLE I
SUMMARY OF THE METHODS IN THE COIL COMBINATION SIMULATION

	B_1 magnitude estimation	B_1 phase estimation	B_1 , T_1 , T_2 , spin density
"method 1"	Phantom (off-line)	Phantom (off-line)	Uniform maps
"method 2"	Phantom (off-line)	Low-res <i>in-vivo</i> (online)	Uniform maps
"oracle method"	True B_1 magnitude	True B_1 phase	True maps

one may argue that the phase mapping scans are collected anyway in "method 2" of the coil combination optimization. However, the coil combination optimization and the regularized reconstruction are independent methods. When one only needs the regularized method and uses a previously optimized coil combination, the proposed B_1 mapping method does avoid the B_1 phase scans. If one needs both regularized method and coil combination optimization, it may seem redundant to collect B_1 phase twice, but the resolution of the B_1 phase collected for "method 2" may be too low for pulse design. In addition, for 3D B_1 mapping, one may need only one or a few low resolution 2D B_1 phase maps for "method 2", whereas a full 3D phase map may be needed for pulse design.

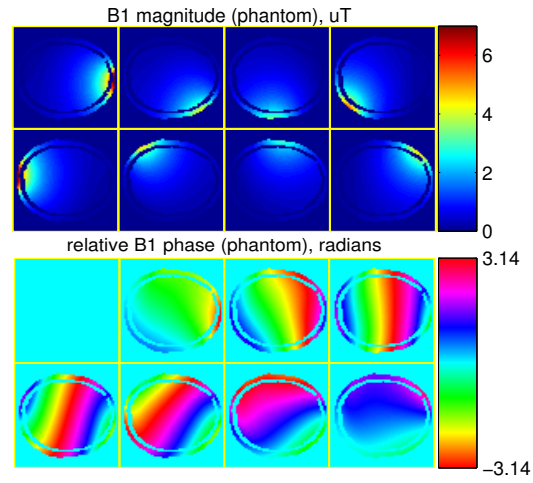


Fig. 4. B_1 maps of the phantom (masked by the brain shape), used for optimizing the coil combinations.

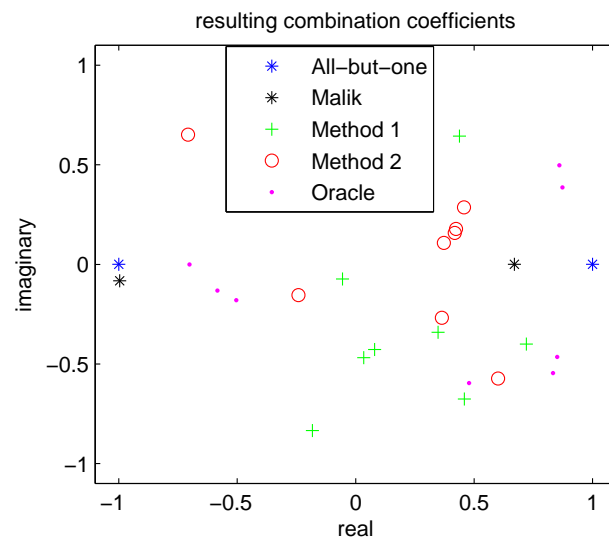


Fig. 5. The first row of the coil combination matrices designed by different methods, where the magnitude is normalized to the peak nominal power of the system.

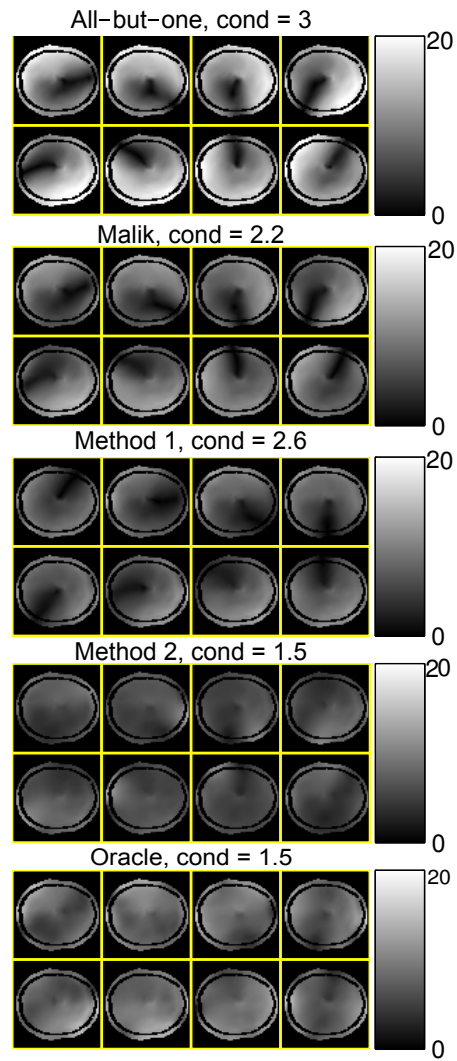


Fig. 6. Magnitude of the composite B_1 maps (masked), $\tilde{B}_n(\mathbf{r})$, by different methods, in μT . The condition numbers (cond) of the coil combination matrices are shown on the titles.

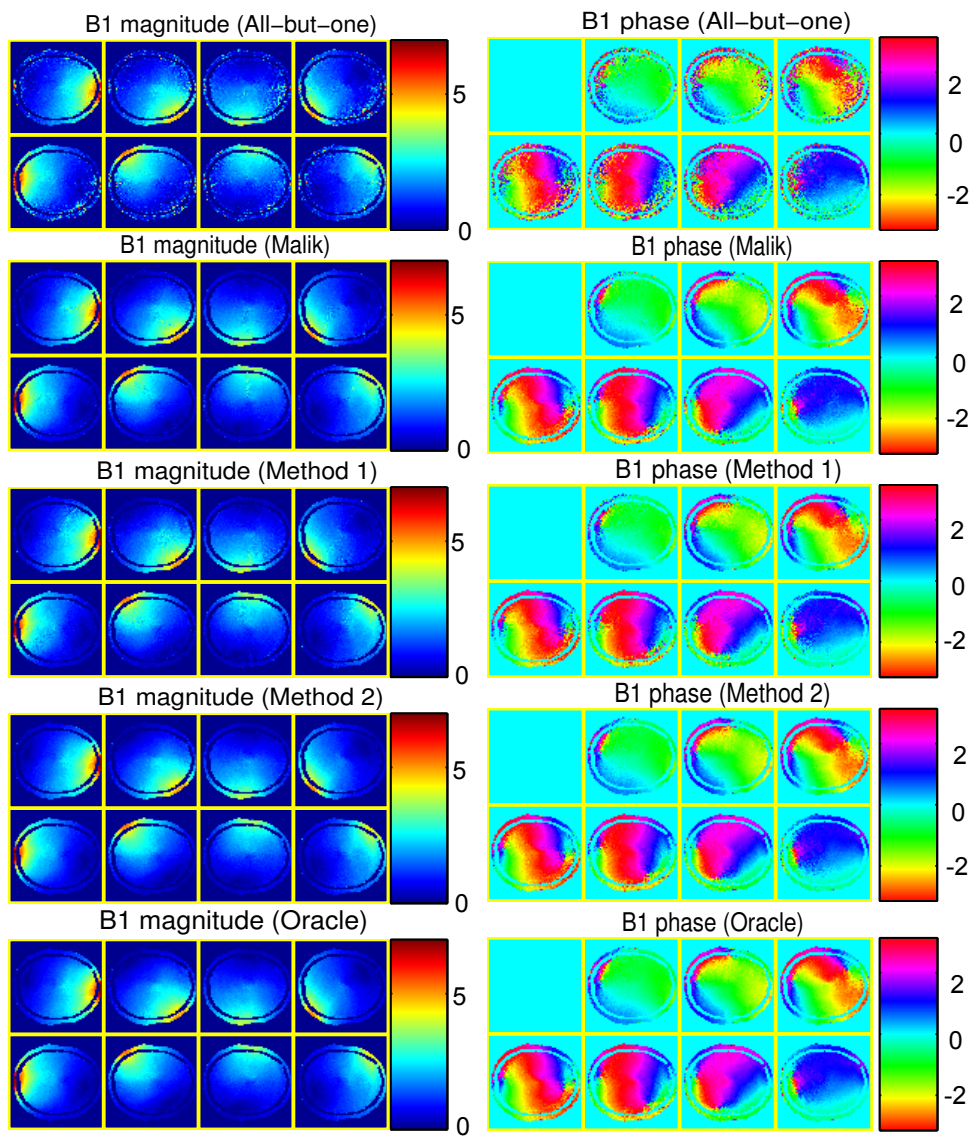


Fig. 7. The simulation results of all the methods; left: B_1 magnitude estimates (in μT), right: relative B_1 phase estimates (in radians).

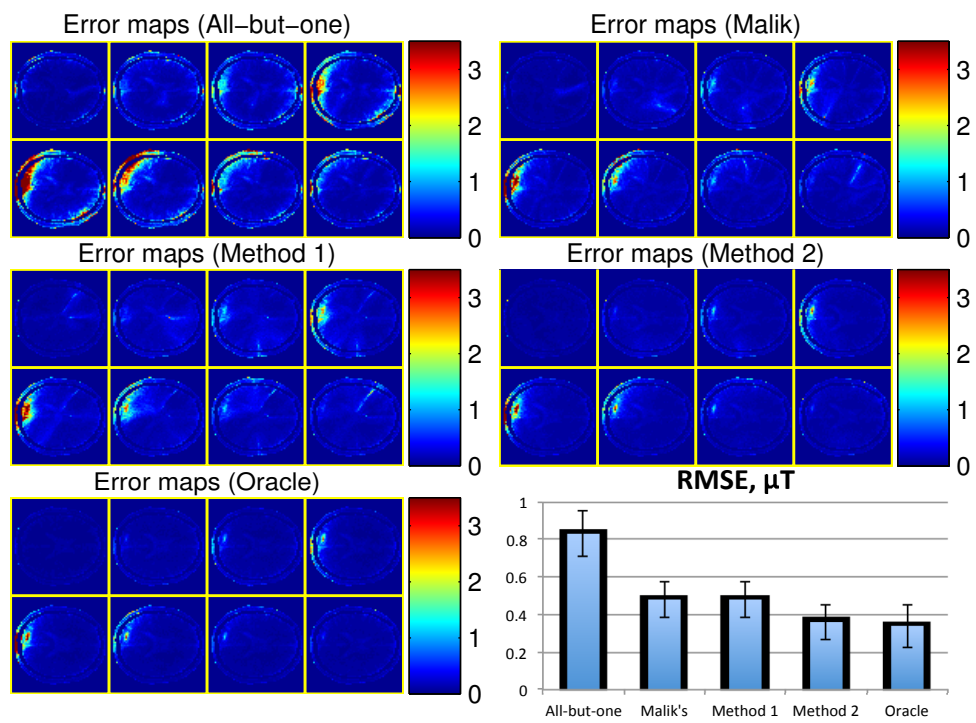


Fig. 8. The error maps of the estimated complex B_1 maps (in μT) of all the methods and the corresponding RMSEs.

Our simulation study shows that the optimization results are relatively insensitive to accuracy of T_1 , T_2 , spin densities, receive sensitivities and B_1 magnitude for 3T brain imaging. Among these magnitude related parameters, the simulation results were more sensitive to different T_1 values (results not shown). We empirically found that using uniform maps with the maximal T_1 is generally more robust than using other T_1 values for this T_1 weighted SPGR-based BS sequence. As B_1 phase of the phantom is likely to be far from the *in-vivo* B_1 phase, we prefer "method 2" which requires only minimal additional scan time. An alternative to "method 2" would be to compute a library of optimized coil combinations for different imaging anatomies and store them offline. This will require a thorough study about the reproducibility of each optimized coil combination across subjects for each imaging anatomy.

The highly nonlinear and nonconvex coil combination optimization produces random-like combination coefficients, and is highly dependent on the initialization and the pseudo-random seeds used in the SA algorithm, so they are probably not global minimums. However, as we only need to find some combination coefficients that improve the raw data, rather than being the very best choice, the proposed coil combination optimization method is still useful in practice. Even so, further investigations on faster or more robust nonlinear optimization algorithms for this challenging optimization problem will be interesting future work.

Although the optimized coil combination works in practice, this CRLB analysis is only an approximation because the MLE of B_1 magnitude and phase are biased estimators in general. Even more estimation bias can be introduced from regularization. Thus, future work could be to design a coil combination optimization based on the biased CRLB analysis [26] which is theoretically valid for regularized estimation.

Although good estimates of B_1 maps may be achieved with the all-but-one combinations using the regularized estimation, the proposed coil combinations produce raw data with much better SNR, improving robustness of the regularized estimation method. Sometimes, the optimized coil combination yields adequate B_1 estimates without requiring regularization, which may be preferable for practical use.

The proposed coil combination optimization does not constrain specific absorption rate (SAR), which could be a concern in BS B_1 mapping sequences. Applying complex weights to PEX channels may cause unpredictable local SAR increase depending on local electromagnetic properties of the tissue [27], so future work can be to consider SAR limits in the coil combination optimization, especially for high field PEX B_1 mapping. One could validate that the resulting sequences are within the relevant local SAR limits after the optimization stage, based on local SAR models, e.g., those proposed in [28]–[30]. A better solution would be to incorporate some SAR limit terms or SAR penalty terms to (16), so that SAR constraints can be considered in the coil optimization stage. Although the unconstrained coil combination optimization may produce SAR problems, the optimization framework provides opportunities for SAR reduction by providing more degrees of freedom for SAR optimized BS pulse design compared to conventional leave-one-out methods.

The simulations for the coil combination optimization used the 2D SPGR sequence, but similar principles can be easily applied for other typical 2D or 3D BS B_1 mapping compatible sequences. In addition, improving coil combination is generally important to other multi-coil B_1 mapping methods, including both phase-based and magnitude-based methods. Although the proposed method was developed for BS B_1 mapping, the framework of the CRLB based coil combination optimization can be applied to other popular multi-coil B_1 mapping methods, e.g., AFI [2].

APPENDIX

This appendix shows the detailed derivation for the CRLB analysis discussed in section II.E. Following (14), we can get the log-likelihood, $L(\boldsymbol{\theta})$, and its gradient:

$$L(\boldsymbol{\theta}) = -\frac{1}{2\sigma^2}(\mathbf{y} - \boldsymbol{\mu}(\boldsymbol{\theta}))^H(\mathbf{y} - \boldsymbol{\mu}(\boldsymbol{\theta})) \quad (19)$$

$$\nabla L(\boldsymbol{\theta}) = \frac{1}{\sigma^2}[\nabla \boldsymbol{\mu}(\boldsymbol{\theta})]\boldsymbol{\epsilon} \quad (20)$$

where the superscript H denotes Hermitian transpose, and ∇ denotes column gradient of vectors. Thus, the estimation satisfies the regularity condition, i.e., $E(\nabla L(\boldsymbol{\theta})) = \mathbf{0}$. The Fisher information $F(\boldsymbol{\theta})$ of this model is:

$$F(\boldsymbol{\theta}) \triangleq E[(\nabla L(\boldsymbol{\theta}))(\nabla L(\boldsymbol{\theta}))^H] = \frac{2M^2}{\sigma^2} \begin{bmatrix} 4K^2 B^2 & 0 \\ 0 & 1 \end{bmatrix}. \quad (21)$$

According to CRLB, if the estimators $[\hat{B}, \hat{\phi}]$ are unbiased, their covariance has a lower bound:

$$\text{cov}([\hat{B}, \hat{\phi}]) \geq F(\boldsymbol{\theta})^{-1}. \quad (22)$$

Assuming \hat{B} and $\hat{\phi}$ are close to the true values, the variance of $\hat{B}e^{i\hat{\phi}}$ can be derived by Taylor expansion approximation. For an arbitrary multi-dimensional function $g(\mathbf{z})$, we have:

$$g(\mathbf{z}) \approx g(\bar{\mathbf{z}}) + \nabla g(\bar{\mathbf{z}})(\mathbf{z} - \bar{\mathbf{z}}) \quad (23)$$

$$\text{var}(g(\mathbf{z})) \approx \nabla g(\bar{\mathbf{z}})\text{cov}(\mathbf{z})\nabla g(\bar{\mathbf{z}})^H \quad (24)$$

so if $\mathbf{z} = (\hat{B}, \hat{\phi})$, $g(\mathbf{z}) = \hat{B}_n e^{i\hat{\phi}}$, $\nabla g(\bar{\mathbf{z}}) = E[e^{i\phi}, iBe^{i\phi}]$, and (22) are plugged into (24), we have:

$$\text{var}(\hat{B}_{n,r}(A)e^{i\hat{\phi}'_{n,r}(A)}) \geq \frac{\sigma^2}{2M_{n,r}^2(A)} [\tilde{B}_{n,r}^2(A) + \frac{1}{4K^2 \tilde{B}_{n,r}^2(A)}] \quad (25)$$

where we have put back the subscripts n , indices \mathbf{r} , primes and tildes in (5) except that we put indices \mathbf{r} to the subscripts and make A be the argument, as A is the main unknown of this optimization problem.

Assuming that noise in different scans is independent, the covariance of the estimated composite B1 maps $\hat{C}_{\mathbf{r}}(A) \triangleq [\hat{B}_{1,\mathbf{r}}(A)e^{i\hat{\phi}'_{1,\mathbf{r}}(A)}, \dots, \hat{B}_{N,\mathbf{r}}(A)e^{i\hat{\phi}'_{N,\mathbf{r}}(A)}]$ is:

$$\text{cov}(\hat{C}_{\mathbf{r}}(A)) = \text{diag}\{\text{var}(\hat{B}_{n,\mathbf{r}}(A)e^{i\hat{\phi}'_{n,\mathbf{r}}(A)})\}. \quad (26)$$

Using (9), the covariance of the original individual B_1 estimates $\hat{C}_{\mathbf{r}}(A) \triangleq [\hat{B}_{1,\mathbf{r}}(A)e^{i\hat{\phi}'_{1,\mathbf{r}}(A)}, \dots, \hat{B}_{N,\mathbf{r}}(A)e^{i\hat{\phi}'_{N,\mathbf{r}}(A)}]$ is:

$$\text{cov}(\hat{C}_{\mathbf{r}}(A)) = A^{-1}\text{cov}(\hat{C}_{\mathbf{r}}(A))A^{-H} \quad (27)$$

where $z^{-H} \triangleq (z^{-1})^H$. Since the diagonal entries of the covariance matrix are the variances of the elements of the estimator, plugging in (25) and (26) into (27) yields the key formula of this CRLB analysis, which is (15).

ACKNOWLEDGMENT

The authors would like to thank N. Hollingsworth and K. Moody from Texas A & M University for providing the parallel excitation system, J. Rispoli from Texas A & M University for helping on the B_1 map simulation, Dr. J.-F. Nielsen from The University of Michigan for his help in the pulse sequence programming, Dr. D. Yoon from Stanford University and the reviewers for useful suggestions.

REFERENCES

- [1] E. Insko and L. Bolinger, "Mapping of the radiofrequency field," *Journal of Magnetic Resonance, Series A*, vol. 103, no. 1, pp. 82–85, 1993.
- [2] V. Yarnykh, "Actual flip-angle imaging in the pulsed steady state: A method for rapid three-dimensional mapping of the transmitted radiofrequency field," *Magnetic resonance in Medicine*, vol. 57, no. 1, pp. 192–200, 2007.
- [3] L. Sacolick, F. Wiesinger, I. Hancu, and M. Vogel, "B1 mapping by Bloch-Siegert shift," *Magnetic Resonance in Medicine*, vol. 63, no. 5, pp. 1315–1322, 2010.
- [4] L. Sacolick, G. W. A., G. Kudielka, W. Loew, and M. W. Vogel, "Interference Bloch-Siegert B1 mapping for parallel transmit," in *Proceedings of the 19th Scientific Meeting of International Society for Magnetic Resonance in Medicine, Montreal, Canada*, 2011, p. 2926.
- [5] K. Nehrke and P. Bornert, "Improved B1-mapping for multi rf transmit systems," in *Proceedings of the 16th Scientific Meeting of International Society for Magnetic Resonance in Medicine, Toronto, Canada*, 2008, p. 353.
- [6] D. Brunner and K. Pruessmann, "B 1+ interferometry for the calibration of rf transmitter arrays," *Magnetic Resonance in Medicine*, vol. 61, no. 6, pp. 1480–1488, 2009.
- [7] S. Malik, D. Larkman, and J. Hajnal, "Optimal linear combinations of array elements for B1 mapping," *Magnetic Resonance in Medicine*, vol. 62, no. 4, pp. 902–909, 2009.
- [8] F. Zhao, J. Fessler, J.-F. Nielsen, and D. Noll, "Regularized estimation of magnitude and phase of multiple-coil B1 field via Bloch-Siegert B1 mapping," in *Proceedings of the 20th Scientific Meeting of International Society for Magnetic Resonance in Medicine, Melbourne*, 2012, p. 2512.
- [9] F. Zhao, J. A. Fessler, S. M. Wright, J. V. Rispoli, and D. C. Noll, "Optimized linear combinations of channels for complex multiple-coil B1 field estimation with Bloch-Siegert B1 mapping in MRI," in *Biomedical Imaging: From Nano to Macro, 2013 IEEE International Symposium on*. IEEE, 2013, pp. 942–945.
- [10] S. Kirkpatrick, C. Gelatt, and M. Vecchi, "Optimization by simulated annealing," *science*, vol. 220, no. 4598, p. 671, 1983.
- [11] D. Brunner and K. Pruessmann, "A matrix approach for mapping array transmit fields in under a minute," *Quadrature*, vol. 60, no. 80, p. 100, 2008.
- [12] J. Hua, C. Jones, J. Blakeley, S. Smith, P. van Zijl, and J. Zhou, "Quantitative description of the asymmetry in magnetization transfer effects around the water resonance in the human brain," *Magnetic Resonance in Medicine*, vol. 58, no. 4, pp. 786–793, 2007.
- [13] F. Zhao, D. Noll, J. Nielsen, and J. Fessler, "Separate magnitude and phase regularization via compressed sensing," *Medical Imaging, IEEE Transactions on*, vol. 31, no. 9, pp. 1713–1723, 2012.
- [14] K. Lange, *Numerical analysis for statisticians*. Springer, 2010.
- [15] [Online]. Available: <http://www.bic.mni.mcgill.ca/brainweb/>
- [16] C. Cocosco, V. Kollokian, K. Kwan, G. Pike *et al.*, "Brainweb: Online interface to a 3D MRI simulated brain database," 1997.
- [17] R. Kwan, A. Evans, and G. Pike, "MRI simulation-based evaluation of image-processing and classification methods," *Medical Imaging, IEEE Transactions on*, vol. 18, no. 11, pp. 1085–1097, 1999.
- [18] R. Kwan, A. Evans, and Pike, "An extensible MRI simulator for post-processing evaluation," in *Visualization in Biomedical Computing*. Springer, 1996, pp. 135–140.
- [19] D. Collins, A. Zijdenbos, V. Kollokian, J. Sled, N. Kabani, C. Holmes, and A. Evans, "Design and construction of a realistic digital brain phantom," *Medical Imaging, IEEE Transactions on*, vol. 17, no. 3, pp. 463–468, 1998.
- [20] N. Hollingsworth, K. Moody, J. Nielsen, D. Noll, M. McDougall, and S. Wright, "Tuning ultra-low output impedance amplifiers for optimal power and decoupling in parallel transmit MRI," in *Biomedical Imaging: From Nano to Macro, 2013 IEEE International Symposium on*. IEEE, 2013.
- [21] K. L. Moody, N. A. Hollingsworth, J.-F. Nielsen, D. Noll, M. P. McDougall, and S. M. Wright, "Eight-channel transmit/receive head array for use with ultra-low output impedance amplifiers," in *Biomedical Imaging: From Nano to Macro, 2013 IEEE International Symposium on*. IEEE, 2013.
- [22] C. M. Collins, Z. Wang, W. Mao, J. Fang, W. Liu, and M. B. Smith, "Array-optimized composite pulse for excellent whole-brain homogeneity in high-field mri," *Magnetic Resonance in Medicine*, vol. 57, no. 3, pp. 470–474, 2007.
- [23] E. M. Haacke, R. W. Brown, M. R. Thompson, and R. Venkatesan, *Magnetic resonance imaging: physical principles and sequence design*. Wiley-Liss New York, 1999, vol. 1.
- [24] J. Fessler and S. Booth, "Conjugate-gradient preconditioning methods for shift-variant PET image reconstruction," *Image Processing, IEEE Transactions on*, vol. 8, no. 5, pp. 688–699, 1999.
- [25] A. Funai, J. Fessler, D. Yeo, V. Olafsson, and D. Noll, "Regularized field map estimation in MRI," *Medical Imaging, IEEE Transactions on*, vol. 27, no. 10, pp. 1484–1494, 2008.
- [26] A. O. Hero III, J. A. Fessler, and M. Usman, "Exploring estimator bias-variance tradeoffs using the uniform CR bound," *Signal Processing, IEEE Transactions on*, vol. 44, no. 8, pp. 2026–2041, 1996.
- [27] L. Alon, C. M. Deniz, R. Brown, D. K. Sodickson, and Y. Zhu, "Method for in situ characterization of radiofrequency heating in parallel transmit MRI," *Magnetic Resonance in Medicine*, 2012.
- [28] Y. Zhu, L. Alon, C. M. Deniz, R. Brown, and D. K. Sodickson, "System and sar characterization in parallel rf transmission," *Magnetic Resonance in Medicine*, vol. 67, no. 5, pp. 1367–1378, 2012.
- [29] U. Katscher, T. Voigt, C. Findekklee, P. Vernickel, K. Nehrke, and O. Dossel, "Determination of electric conductivity and local sar via b1 mapping," *Medical Imaging, IEEE Transactions on*, vol. 28, no. 9, pp. 1365–1374, 2009.
- [30] J. Liu, X. Zhang, P.-F. Van de Moortele, S. Schmitter, and B. He, "Determining electrical properties based on b1 fields measured in an mr scanner using a multi-channel transmit/receive coil: a general approach," *Physics in medicine and biology*, vol. 58, no. 13, p. 4395, 2013.

Regularized Estimation of Magnitude and Phase of Multi-Coil B_1 Field via Bloch-Siegert B_1 Mapping and Coil Combination Optimizations: Supplementary Material

Feng Zhao*, *Student Member, IEEE*, Jeffrey A. Fessler, *Fellow, IEEE*, Steven M. Wright, *Fellow, IEEE*, and Douglas C. Noll, *Senior Member, IEEE*

This document contains supplementary data and discussions about the conventional low-pass filtering (LPF) methods for B_1 estimation versus the proposed regularized B_1 estimation. The purpose of this document is to confirm the proposed B_1 estimation for the readers who may question the advantages of the regularized methods over the conventional LPF methods.

An important benefit of using regularized methods combined with an appropriate log-likelihood is that such methods have very little error propagation that would be caused by conventional LPF. The key difference is that the low-pass filters are applied to the noisy data whereas the finite differences in the regularizer are applied to the (smooth) estimated B_1 map. LPF methods typically weight the neighboring pixels differently only according to their relative distances to the central pixel, causing the corrupted values in the regions with low magnitudes to propagate errors to the neighboring regions. In contrast, the regularized methods handle this problem by balancing the data fidelity and the prior knowledge differently according to the magnitude of each pixel. This can be understood from the cost function of a regularized method, e.g., equation (7) in the paper. For pixels with lower magnitudes, the data fidelity terms can be very small or trivial compared to the corresponding regularization terms, so the cost function then emphasizes promoting smoothness rather than data fidelity; for pixels with higher magnitudes, the function emphasizes data fidelity. Hence, the method automatically adjusts its weights for data fidelity and prior knowledge (smoothness in our case) according to the reliability (magnitude in our case) of the data. Therefore, the regularized method produces smooth B_1 fields in the corrupted low magnitude regions without corrupting the neighboring regions. From a mathematical point of view, the regularized methods avoid error propagation simply because

lower cost function values can be reached with the smooth non-error-propagated results.

In addition, the proposed regularized method also uses physical and statistical models. The data fidelity term is formed based on the physics of MRI and Bloch-Siegert effect, but LPF does not consider this. So LPF methods may uncontrollably produce systematic errors in the smoothed regions. In addition, the proposed method uses the statistical distributions of the noise, i.e., independent and identically distributed random Gaussian noise, which is essential for promoting the data fidelity. In contrast, LPF methods may not consider that correctly.

There are several options for doing LPF in this problem. First, one can simply smooth the raw data. This is a typical way to denoise an image that has white noise. However, as both B_1 magnitude and phase information are in the phase images, the B_1 estimates are unreliable in regions with low intensities even if low-pass filters are applied. Basically, this smoothing method cannot accurately smooth B_1 maps in those regions. Second, one may smooth the complex B_1 maps formed by the B_1 magnitude and B_1 phase reconstructed using non-regularized methods. This method does not work well, as the noise in these complex images is not white noise any more, which can produce significant systematic error as shown in the results below. Last, one may smooth the magnitude and phase components of the complex B_1 separately. For the phase part, ϕ , we smooth the exponential of the phase, i.e., $e^{i\phi}$, instead of the phase itself, to avoid phase wrapping. In the end, the smoothed $e^{i\phi}$ needs to be normalized to have unit magnitude before recombining with the smoothed magnitude parts.

We applied the three LPF methods mentioned above to the B_1 estimates produced by the standard non-regularized method in the simulations (Section II.D) and the phantom experiment (Section II.E) in the paper. In our implementations, we manually tuned the low-pass filter parameters and show the best results in this document. The results of these LPF methods are compared with the results of the non-regularized method and the regularized method shown in the paper (Fig. 2 and Fig. 3).

Fig. S-1 shows the LPF results of the simulation data, where the left column shows the method that filters the raw data, the middle column shows the method that filters the complex B_1 , and the right column shows the method that

This work was supported in part by the National Institutes of Health under Grant R01 NS58576 and Grant P01 CA87634. Asterisk indicates corresponding author.

*F. Zhao is with the Biomedical Engineering Department, The University of Michigan, Ann Arbor, MI 48109, USA (e-mail: zhaofll@umich.edu).

J. A. Fessler is with the Department of Electrical Engineering and Computer Science, The University of Michigan, Ann Arbor, MI 48109, USA (e-mail: fessler@umich.edu).

S. M. Wright is with the Department of Electrical and Computer Engineering, Texas A& M University, College Station, TX 77843, USA (e-mail: smwright@tamu.edu).

D. C. Noll is with the Biomedical Engineering Department, The University of Michigan, Ann Arbor, MI 48109, USA (e-mail: dnoll@umich.edu).

filters the magnitude and phase parts. The top two rows show the B_1 magnitude and phase maps for one instance of random noise, and the bottom row shows the error maps between the reconstructed complex B_1 fields and the ground truth, where each pixel value is the average error magnitude over the 20 instances of random noise. As expected, the left column results have less systematic error than the other two LPF methods due to better statistical modeling of the noise, but this LPF method introduces large error propagation in low magnitude regions, e.g., the center regions, between neighboring pixels and also between channels due to the coil combinations. The other two LPF methods are not based on the correct statistical models and physical models, so they smoothed out some noise but tend to introduce severe systematic errors, especially around the skull region. All those visual observations are consistent with the RMSEs (averaged over the 20 instances of random noise) shown on the figure titles at the bottom row. Although the left column LPF method has a slightly lower $RMSE_1$ and slightly higher $RMSE_2$ compared to the regularized results in Fig. 2, the latter still shows superior visual appearance than the left column in Fig. S-1 that has large areas of error propagations

Fig. S-2 shows the results of the two LPF methods applied to the phantom experiment, and still the left column shows the method that filters the raw data, the middle column shows the method that filters the complex B_1 , and the right column shows the method that filters the magnitude and phase parts. The error propagation in the top row is not as severe as in the simulation, but the low magnitude regions are not smoothed sufficiently by the low-pass filter and are still noisy. Similar to in the simulation, the other two LPF methods show significant systematic errors around the object boundaries.

By comparison, the proposed regularized method shows superior performance (Fig. 2 and Fig. 3 in the paper) than these LPF methods in both the simulations and the phantom experiment.

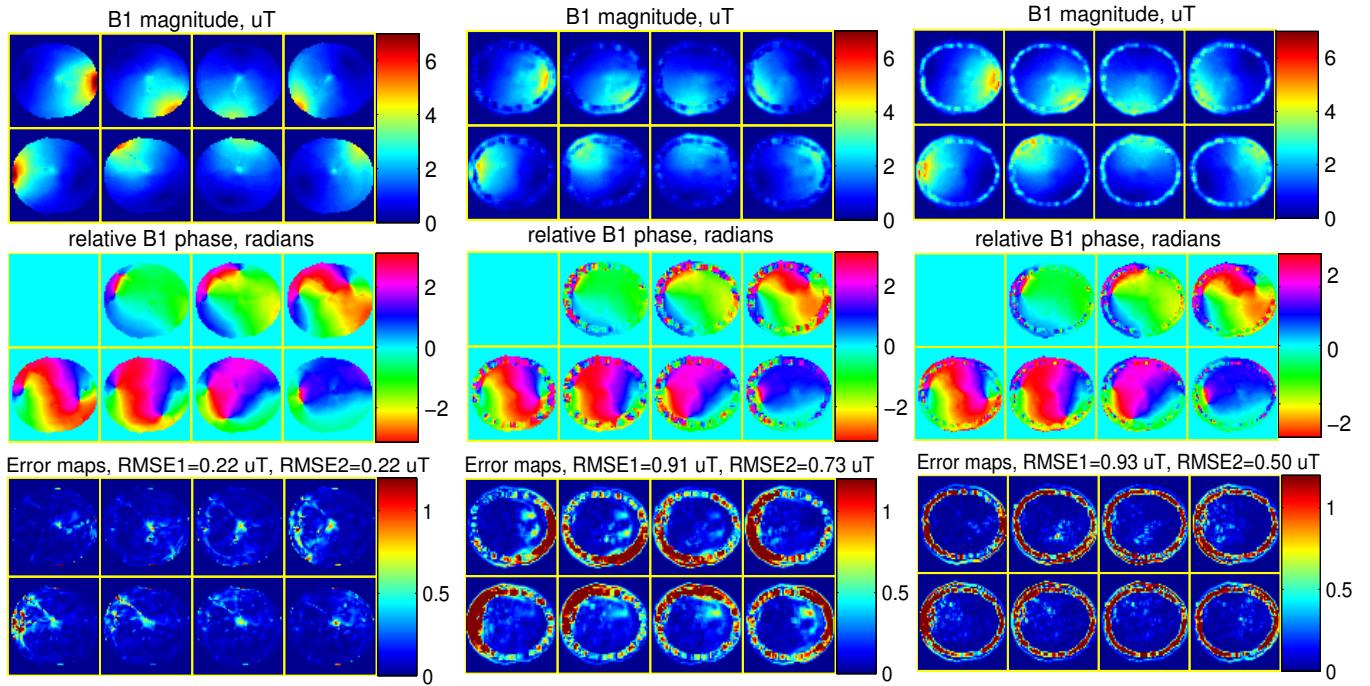


Fig. S-1. The LPF results of the simulation study. These results may be compared with Fig. 1 (ground truth) and Fig. 2 (non-regularized results and regularized results) in the paper. We show the results by the method that filters the raw data (left column), the method that filters the complex B_1 (middle column), and the method that filters the magnitude and phase parts (right column). The top, middle and bottom row show the magnitude, phase and error maps (with average RMSEs on the titles), respectively.

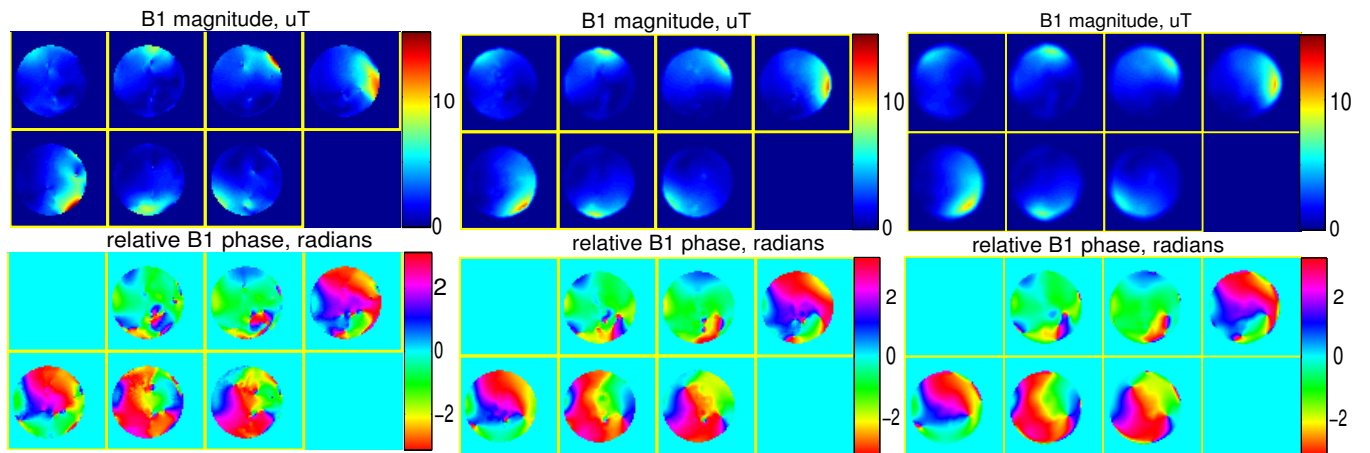


Fig. S-2. The LPF results of the phantom experiment. These results may be compared with Fig. 3 (non-regularized results and regularized results) in the paper. We show the results by the method that filters the raw data (left column), the method that filters the complex B_1 (middle column), and the method that filters the magnitude and phase parts (right column).